DUP

UGR #C162 7903

UCRL-50036-79-3

LLL gas stimulation program quarterly progress report July through September 1979

M. E. Hanson, G. D. Anderson,
R. J. Shaffer, D. F. Towse,
J. R. Hearst, W. Lin, and M. P. Cleary

November 28, 1979

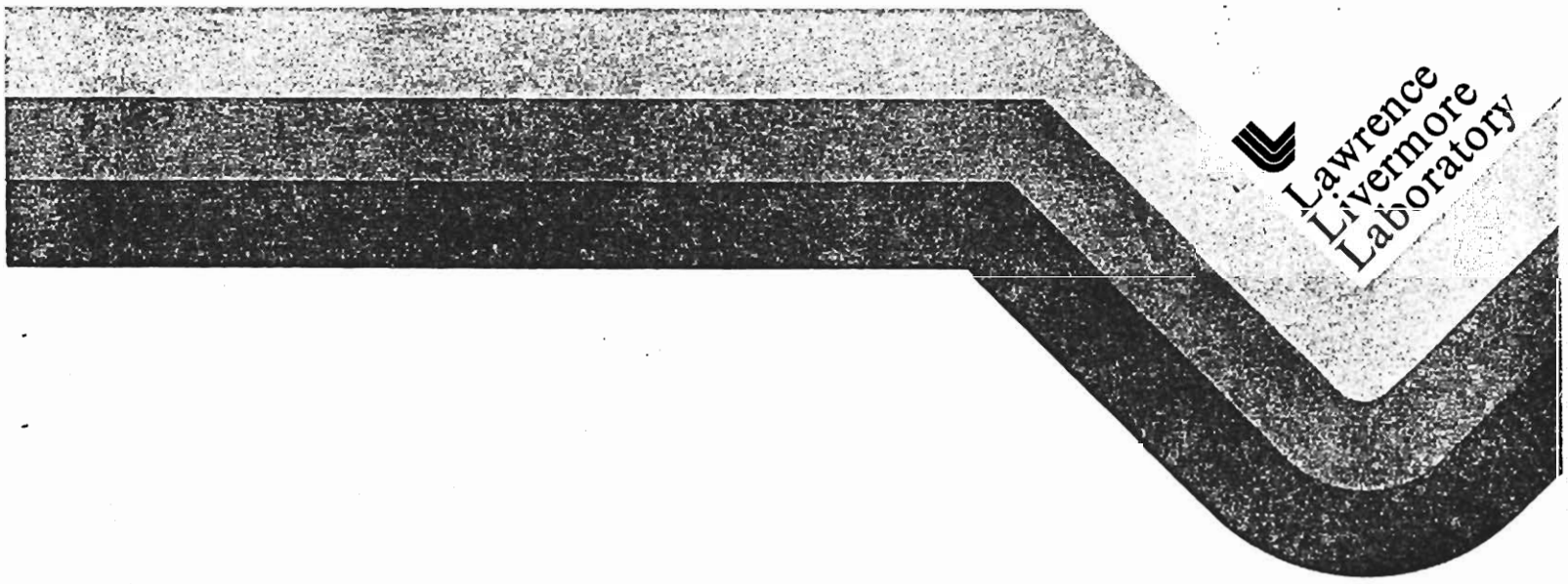

Work performed under the auspices of the U.S. Department of Energy by the Lawrence Livermore Laboratory under Contract W-7405-Eng-48.

UCRL-50036-79-3
Distribution Category UC-92a

LLL gas stimulation program quarterly progress report July through September 1979

M. E. Hanson, G. D. Anderson,
R. J. Shaffer, D. F. Towse,
J. R. Hearst, W. Lin, and M. P. Cleary*

Manuscript date: November 28, 1979

*Massachusetts Institute of Technology, Cambridge, Massachusetts.

LAWRENCE LIVERMORE LABORATORY
University of California • Livermore, California • 94550

PREFACE

Although U.S. gas resources remain large, proven reserves have declined to 230 trillion feet, and the current reserves/production ratio is 10 to 1.

It is estimated that tight (i.e., low-permeability) western gas reservoirs and eastern Devonian gas shales contain large quantities of natural gas, but because of the low permeability, these resources have been difficult to recover. Some gas has been produced, but industry needs more economical recovery techniques. The region around the production wells must be stimulated in some manner to induce a more rapid flow into the well bore. The stimulation process involves creating channels or cracks out into the reservoir from the well bore. This can be done by detonating high explosives or nuclear explosives in the well bore or by hydraulically fracturing the formation.

Currently, the most promising techniques for stimulating low-permeability gas reservoirs are hydraulic fracturing and massive hydraulic fracturing (MHF). Hydraulic fracturing involves pumping fluids under high pressure down the well bore and out into the reservoir. The hydraulic action fractures the rock around the well bore, and proppants in the fracturing fluids hold the cracks open. The fractures provide large drainage faces for the gas and channel it into the well bore. Hydraulic fracturing has been routinely used in oilwell completion and cleanup for many years. MHF differs from hydraulic fracturing in that larger amounts of fluid and proppant are pumped down the well to create and prop fractures at much greater distances.

The application of MHF techniques to tight western gas formations has given variable and sometimes disappointing results. The best efforts of a CER-led industry/government consortium to stimulate the Piceance Basin near Rio Blanco, Colorado, were not successful. On the other hand, Amoco has used MHF techniques in the Wattenburg field near Denver with a high degree of success. Significant differences in the reservoirs themselves apparently account for the differences in success.

The Devonian shales present similar problems. It is believed that production from these gas shales results from the connection of the wells to the existing fracture patterns. Hence, to recover this gas, we must locate the producing zones, locate the natural fractures near the well bore, and fracture from the well bore to the existing fractures.

The Lawrence Livermore Laboratory (LLL) has embarked on a research program to help develop tight gas reservoirs in the United States. We are trying to obtain a more detailed understanding of the stimulation processes, including how the formation properties interact with and affect these processes. The problem is to determine how to connect the maximum amount of productive reservoir rock to the well bore through a highly permeable fracture system.

There are several questions that we would like to be able to answer in advance about the tight Rocky Mountain formations. Can we identify particular sections where the fractures may be expected to be preferentially confined to the productive sands, so that a maximum volume of reservoir can be stimulated? What is the geometry (length, width, and number) of the fractures? What is the nature of the treatment (fluid composition, volumes, pumping rates, perforation intervals) which, when applied to a formation with certain properties, will result in optimum and economical recovery? What are some of the important geophysical measurements and experiments that can aid in this endeavor? What data and experiences exist that are relevant? Most of the western reservoirs contain a high degree of water saturation, which can significantly reduce the already low permeability of these reservoirs; it is possible to use existing logging techniques supplemented by new geophysical measurements to ascertain the *in situ* water saturation?

Devonian shales present many of the same challenges as the tight Rocky Mountain formations. There are, however, some special problems. Logging techniques for these shales are just being developed, and we have not yet acquired the ability to locate the fractures that do not intersect the well bore. The effect of hydraulic fracturing on Devonian shales is also not well understood. Water, one of the standard hydraulic fracturing fluids, can cause significant formation damage; organic and cryogenic fluids are expensive; high-explosive fracturing makes well clean-out and completion costly and uncertain; and, as we have shown previously,[1] the diameter of permeability enhancement is small.

Our program is primarily investigative. We are not currently proposing any field programs. We are, however, constructing and applying theoretical models and performing laboratory experiments to develop an

understanding of the gas stimulation process. These tasks are complementary, and parallel development is necessary. Another facet of the program is geophysical measurement (logging) in the environments where these stimulation processes are applied. Close association with the DOE-supported field programs provides the interaction and direction necessary to the program.

The LLL program can be broken into eight task areas: (1) theoretical modeling of the hydraulic fracturing process; (2) laboratory hydraulic fracturing experiments; (3) log tool development and analysis of log data; (4) cataloging and evaluation of pertinent geological and geophysical reservoir data; (5) measurement of pertinent reservoir properties; (6) reservoir analysis; (7) evaluation of other stimulation techniques; and (8) environmental reports in support of DOE field programs.

LLL GAS STIMULATION PROGRAM
Quarterly Progress Report
July through September 1979

ABSTRACT

This report summarizes the research and accomplishments of the LLL Gas Stimulation Program during the third quarter of FY 1979. We have continued to analyze dynamic fracture propagation near interfaces and have begun some analyses to determine the effects of frictional slip along interfaces. Some experiments have been performed to analyze the effects of existing cracks near an interface. These experimental results compare with theoretical predictions. Analyses for the formulation of three-dimensional models have indicated some discretization schemes for development of the numerical models. We have continued the measurement of mechanical properties and failure characteristics of core material from the western tight gas reservoirs. Additionally, we have been applying various schemes, including the use of color plots, to evaluate the data obtained with continuous three-dimensional sonic logs.

THEORETICAL ANALYSES

RESULTS FROM TWO-DIMENSIONAL NUMERICAL MODELS

We have applied our two-dimensional, time-dependent, finite-element model[2,3] to determine the material overshoot characteristics caused by a crack that initiates, propagates bilaterally at half the dilatational wave speed, and stops when one tip reaches a well-bonded interface. The problem geometry is shown in Fig. 1. Note that c is the final half crack length, and we denote the time interval from crack starting to stopping as t_d. The problem is solved in plane strain, and the coordinate system is referenced to the center of the crack. For our current studies the densities of the two materials are set equal (2.7 g/cm^3) and the Lamé constants λ and μ for each material are also equal, so that Poisson's ratio is 0.25 for both materials.

The results of our calculations are shown in Fig. 2. Nondimensional vertical displacement, v/c, is plotted vs nondimensional time, t/t_d, for the point x = 0.8c, y = 0.1c. Three calculations were made, corresponding to three sets of values for the Lamé constants as shown in the figure. The constants μ_1 and λ_1 were kept at 30 GPa for all three calculations so that the center curve corresponds to the homogeneous case. Points of maximum displacement are related to the maximum likelihood of crack reinitiation. We see that interface penetration becomes less likely as the second material becomes stiffer. We also note that the peak displacement occurs earlier as the second material becomes stiffer.

Our equilibrium model[4] was applied to analyze some of the effects of frictional interfaces on a pressurized fracture as the crack propagates toward the interface. Three calculations were performed with these different frictional stresses applied along the interface. The geometry of the fracture and the interface used in the calculations is shown in Fig. 3. The pressure in the crack was constant and the material on both sides of the interface was identical. Material properties on both sides of the interface were identical with a Poisson's ratio equal to 0.25. The ratio of the pressure in the crack to the Young's modulus for the material (P_c/E) was 1.5×10^{-3}. In these calculations we ignored the effects of changes in pore pressure caused by fluid leaking from the crack into the surrounding material.

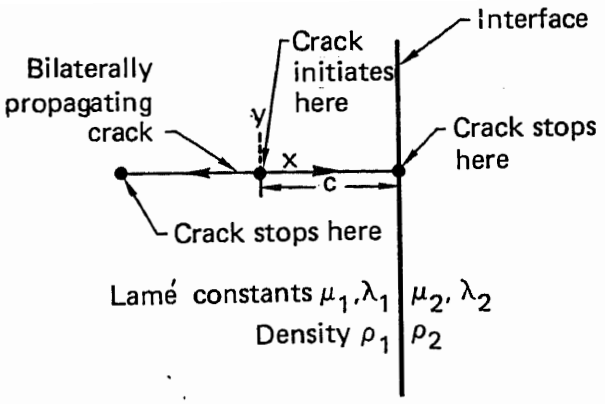

FIG. 1. Geometry of time-dependent crack problem.

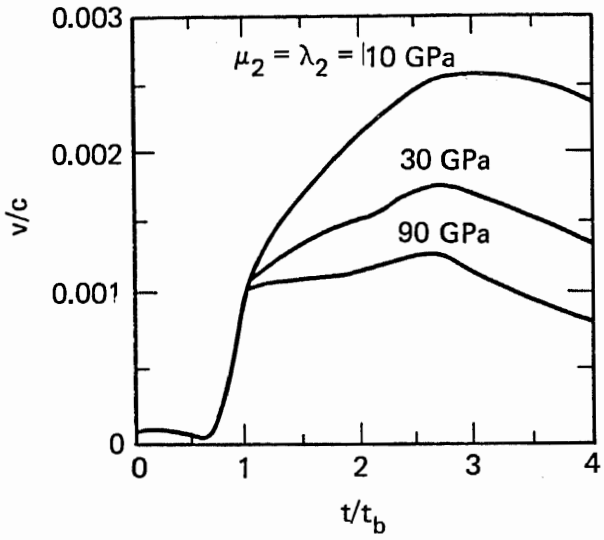

FIG. 2. Displacement in y-direction of point x = 0.8c, y = 0.1c (elastic constants for material 1 are 30 GPa).

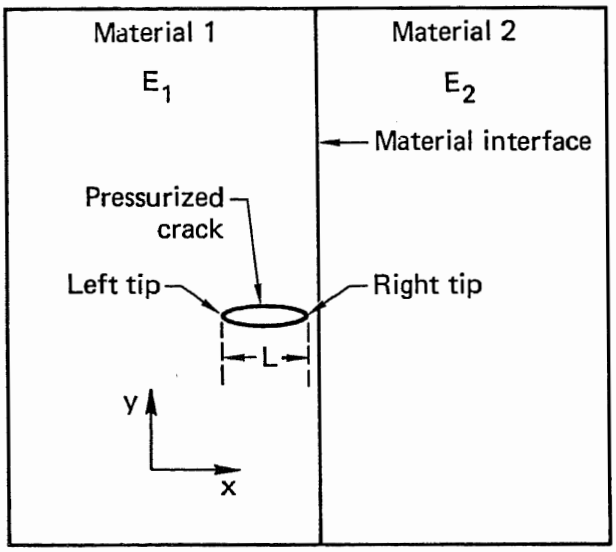

FIG. 3. Geometry of fracture near frictional interface (Note: materials were the same in these calculations).

The results of the calculations are shown in Fig. 4, and for presentation we have scaled the distance of the crack from the interface with the crack length. The ratio of the initial frictional stress to the pressure in the crack, $\gamma = \tau_f/P_c$, for these three sets of calculations was 0.033, 0.067, and 0.1. In these calculations, the crack did not penetrate the interface; hence, we have not attempted to evaluate the frictional conditions for such penetration. However, we are developing experimental data that can provide correlation for these analyses. The results presented show how changes in the interfacial frictional stress tend to enhance or impede fracture propagation toward the interface.

As expected, when the scaled distance from the crack to the interface is greater than one, the effects of the frictional interface on the pressurized crack are small. Relative motion along the interface was seen to increase both as the pressurized fracture approaches the interface and as the frictional coefficient becomes smaller. The frictional stress along the interface changes as the crack nears the interface. The largest change in

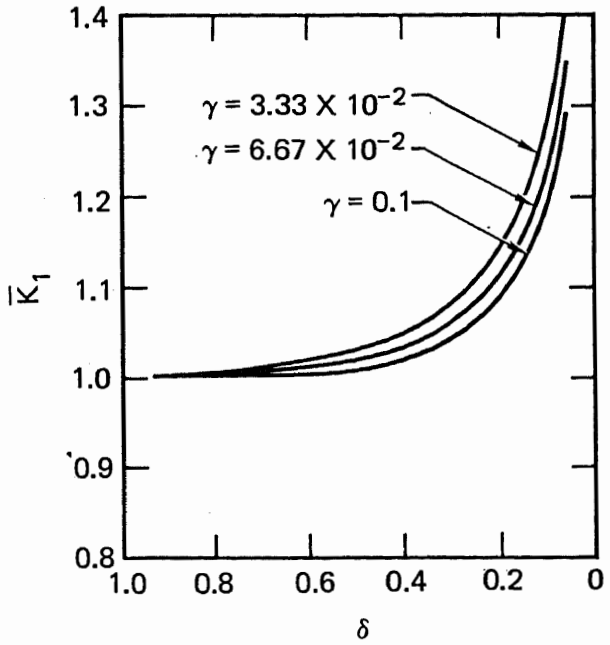

FIG. 4. Variation in Mode I stress-intensity factor as crack approaches frictional interface for variations in frictional stress along interface (see text for definition of variables).

this frictional stress occurs in a region directly ahead of the crack tip where it decreases to very small values when the scaled distance is less than 0.2. As has been done previously,[4] we have scaled the Mode I stress-intensity factor (Fig. 4) with $P_c \sqrt{a}$ where P_c is the pressure in the crack and a is the semimajor axis of the fracture ellipse. Figure 4 shows changes in the scaled Mode I stress-intensity factor (K_I) as the crack tip approaches the interface for the three values of the initial frictional stress on the interface. The stress-intensity factor can be thought of as the tendency to break, and as we see this fraction increase, we should expect fracture propagation to be enhanced. Figure 4 shows that for the lower frictional stresses along the interface, the tendency to break increases more rapidly as the crack approaches the interface. This indicates that the crack is more strongly drawn toward the interface for the lower frictional stresses, a similar tendency as that when there is a lower modulus material to the right of the interface. However, the chance of penetrating the interface decreases with frictional stress comparing with the experimental results.

TRACING OF FRACTURE-FLUID PRESSURE EVOLUTION

Previously we were able to develop numerical procedures stable enough to allow explicit computation of evolving fluid pressure and crack geometry.[5,6] However, the results obtained were inevitably too-little-influenced by the elastic properties of the rock, and were effectively dominated by the requirement of fracture-fluid mass conservation, which dictated the change in width from one step to the next. For this reason we believed it essential to employ a method by which fracture-fluid pressure would be implicitly computed at each time step so as to satisfy simultaneously the requirements of elasticity and mass conservation. Further, because of the success achieved with the dislocation dipole scheme, it was decided to base our implicit method on the latter, rather than on the dislocation density scheme, in order to avoid anticipated trouble with the higher order differentiation.

Thus, we start with the integral equation relating fracture-fluid pressure and dipole density or crack opening displacement δ[1]:

$$p(x_0)/G = \int_{-\ell}^{+\ell} \gamma_D(x_0, x)[\delta(x) - \delta(x_0)]\,dx - \delta(x_0)[\gamma(x_0, \ell) - \gamma(x_0, -\ell)]\,, \tag{1a}$$

where, for a homogeneous isotropic infinite medium,

$$\gamma_D = -1/2\pi(1 - \nu)(x_0 - x)^2 \equiv -d\gamma/dx\,. \tag{1b}$$

Here, γ_D is the influence function that gives the stress at point x_0 due to the difference in dipole strengths δ at points x and x_0, and γ is the analogous influence function associated with dislocations.[4,7] Differentiating Eq. (1a) with respect to time gives (for time-independent γ and stationary crack-tips):

$$\dot{p}(x_0)/G = \int_{-\ell}^{+\ell} \gamma_D(x_0, x)[\dot{\delta}(x) - \dot{\delta}(x_0)]\,dx - \dot{\delta}(x_0)[\gamma(x_0, +\ell) - \gamma(x_0, -\ell)]\,. \tag{2}$$

We have seen earlier[6] that the simplest fluid flow model—Poiseuille flow—gives the result that $\hat{\eta}\dot{\delta} = [\delta^3 p']'$ (here $\hat{\eta}$ denotes an effective viscosity, and we have used G, ν for shear modulus and Poisson's ratio of the surrounding rock; also, the apostrophe denotes spatial differentiation, while the dot indicates differentiation with respect to time). If we now make the following approximations:

$${}^{t}\dot{\delta} = \alpha^{t+\Delta t}\dot{\delta} + (1 - \alpha)^{t}\dot{\delta}, \quad \dot{p} = \frac{{}^{t+\Delta t}p - {}^{t}p}{\Delta t}\,, \tag{3}$$

and substitute into Eq. (2), we get an equation that may be rearranged so that only terms evaluated at time $t+\Delta t$ are on the left and only those at time t are on the right. When we completely nondimensionalize all terms, we get (assuming fluid penetration all the way to the tip; viz., a stationary crack):

$$\begin{aligned} {}^{t+\Delta t}p(x_0) - \frac{\alpha\Delta t}{\tau_c}\int_{-1}^{+1} \gamma_D(x_0, x)\left\{{}^{t+\Delta t}[\delta^3 p']'(x) - {}^{t+\Delta t}[\delta^3 p']'(x_0)\right\}dx \\ + \frac{\alpha\Delta t}{\tau_c}\,{}^{t+\Delta t}[\delta^3 p']'(x_0)[\gamma(x_0, 1) - \gamma(x_0, -1)] \\ = {}^{t}p(x_0) + \frac{(1 - \alpha)\Delta t}{\tau_c}\int_{-1}^{+1} \gamma_D(x_0, x)\left\{{}^{t}[\delta^3 p']'(x) - {}^{t}[\delta^3 p']'(x_0)\right\}dx \\ - \frac{(1 - \alpha)\Delta t}{\tau_c}\,{}^{t}[\delta^3 p']'(x_0)[\gamma(x_0, 1) - \gamma(x_0, -1)]\,, \end{aligned} \tag{4}$$

where it is understood that p and δ are now dimensionless; that is,

$$\delta \leftarrow \frac{G\delta}{p_0\ell}\,, \quad p \leftarrow \frac{p}{p_0}\,, \quad \text{and} \quad \tau_c = \frac{\hat{\eta}}{G}\left(\frac{G}{p_0}\right)^3$$

is the characteristic time predicted by Cleary.[8] The parameter α is chosen to provide the most stable solution; in fact, it will be seen later that the best choice is $\alpha = 1$. If we make the assumption that ${}^{t+\Delta t}\delta = {}^{t}\delta$ (or any other relation between ${}^{t+\Delta t}\delta$ and ${}^{t}\delta$) we can rewrite Eq. (4) as a set of linear algebraic equations by using the appropriate discrete formulas for integration and differentiation. First, we approximate the integrals in Eq. (4) by the Gauss-Chebyshev formula:

$$\int_{-1}^{+1} \gamma_D(x_r, x) \left\{ [\delta^3 p']'(x) - [\delta^3 p']'(x_r) \right\} dx$$

$$= \frac{\pi}{N} \sum_{i=1}^{N} \gamma_D(x_r, t_i) \left\{ [\delta^3 p']'(t_i) - [\delta^3 p']'(x_r) \right\} \sqrt{1 - t_i^2} \ , \tag{5a}$$

$$x_r = -\cos(\pi r/N) \ , \qquad r = 1, \cdots, N-1 \ , \tag{5b}$$

$$t_i = -\cos[\pi(2i-1)/2N] \ , \qquad i = 1, \cdots, N \tag{5c}$$

Since we wish to formulate the equations in terms of p, we need to represent $[\delta^3 p']$ in terms of δ and p. Our previous success in termwise differentiation of a Chebyshev series[5] leads us to use that method here:

$$[\delta^3 p']'(x) = \sum_{j=1}^{M} T_j'(x) \left\{ \frac{4}{\pi^2} \int_{-1}^{+1} \left[\frac{T_j(x)\delta^3(x)}{\sqrt{1-x^2}} \sum_{\ell=1}^{L} T_\ell'(x) \int_{-1}^{+1} \frac{T_\ell(x)p(x)}{\sqrt{1-x^2}} dx \right] dx \right\} . \tag{6}$$

Since we will need to impose two constraints on the solution for ${}^{t+\Delta t}p$ (viz., we will in particular maintain the borehole pressure at some desired value, and ${}^{t+\Delta t}p$ will be such that ${}^{t+\Delta t}\delta|_{-1}^{+1} = 0$) we will have one more equation than unknowns (i.e., N+1 equations, N unknowns) unless we obtain $p(x_r)$ from a set or N+1 points by interpolation. Again we make use of the Chebyshev series:

$$p(x_r) = \sum_{\ell=0}^{L-1} T_\ell(x_r) \left[\frac{2}{\pi} \int_{-1}^{+1} \frac{T_\ell(x)p(x)}{\sqrt{1-x^2}} dx \right] . \tag{7}$$

If we apply the Gauss-Chebyshev integration formula in Eqs. (6) and (7), and substitute into Eq. (5) and thence to Eq. (4), we obtain our system of equations:

$$\sum_{\ell=0}^{L-1} T_\ell(x_r) \sum_{s=1}^{L} \frac{2}{L} T_\ell(t_s) [{}^{t+\Delta t}p(t_s) - {}^{t}p(t_s)]$$

$$- \frac{4\Delta t}{LM\tau_c} \left(\frac{\pi}{N}\right) \sum_{i=1}^{N} \gamma_D(x_r, t_i) \sum_{j=1}^{M} \left[T_j'(t_i) - T_j'(x_r) \right] \sqrt{1 - t_i^2} \sum_{k=1}^{M} T_j(t_k)\delta^3(t_k)$$

$$\times \sum_{\ell=1}^{L} T_\ell'(t_s) \sum_{s=1}^{L} T_\ell(t_s) \left[\alpha {}^{t+\Delta t}p(t_s) + (1-\alpha) {}^{t}p(t_s) \right]$$

$$+ \frac{4\Delta t}{LM\tau_c} \left[\gamma(x_r, 1) - \gamma(x_r, -1) \right] \sum_{j=1}^{M} T_j'(x_r) \sum_{k=1}^{M} T_j(t_k)\delta^3(t_s)$$

$$\times \sum_{\ell=1}^{L} T_\ell'(t_s) \sum_{s=1}^{L} T_\ell(t_s) \left[\alpha {}^{t+\Delta t}p(t_s) + (1-\alpha) {}^{t}p(t_s) \right] = 0 \ . \tag{8a}$$

Here we find it natural to make the following identifications:

$$t_{k,s} = -\cos\left\{ \frac{\pi[2(k,s) - 1]}{2L} \right\}, \quad L \equiv M \ . \tag{8b}$$

Equations (8a) and (8b) may be simplified, and the time required to set up and to solve them reduced, through the use of the following matrices:

$$A_{r\ell} \equiv T_{\ell-1}(x_r) \ , \qquad r = 1, \cdots, N-1; \ell = 1, \cdots, L \ , \tag{9a}$$

$$A'_{\ell s} \equiv \frac{2}{L} T_{\ell-1}(t_s) \ , \qquad s = 1, \cdots, L; \ \ell = 1, \cdots, L \ , \tag{9b}$$

$$B_{rj} \equiv \frac{\pi}{N} \sum_{i=1}^{N} \gamma_D(x_r, t_i) \left[T'_j(t_i) - T'_j(x_r) \right] \sqrt{1 - t_i^2} \ , \tag{9c}$$

$$C_{rj} \equiv T'_j(x_r) \ , \tag{9d}$$

$$C'_{kj} \equiv T'_j(t_k) \ , \qquad k = 1, \cdots, M \tag{9e}$$

$$D_{jk} \equiv \frac{2}{M} T_j(t_k) \ , \tag{9f}$$

$$\Delta_{jk} \equiv \delta^3(t_k) \delta_{jk} \ , \tag{9g}$$

$$E_{k\ell} \equiv T'_\ell(t_k) \ , \tag{9h}$$

$$F_{ls} \equiv \frac{2}{L} T_\ell(t_s) \ , \qquad s = 1, \cdots, L \tag{9i}$$

$$G_{rj} \equiv \delta_{rj} [\gamma(x_r, 1) - \gamma(x_r, -1)] \ , \tag{9j}$$

where

$$\delta_{ij} = \begin{cases} 1 \ , & i = j \\ 0 \ , & i \neq j \end{cases} \ .$$

Our experience with fitting functions by a Chebyshev series indicates that when the series is to be differentiated it is best to transform the function so as to make it pass through the origin and be antisymmetric, and then to retransform the series if necessary.[5] To effect the necessary transformations, we define these matrices:

$$H_{sq} \equiv - \delta_{sq} \ \text{sign} \ (t_s) + \delta_{(L/2)s} \ \text{sign} \ (t_s) \ , \tag{9k}$$

$$S_{ij} \equiv \delta_{ij} + \delta_{(M/2)j} \ \text{sign} \ (t_i) \ , \tag{9l}$$

$$T_{jk} \equiv - \delta_{jk} \ \text{sign} \ (t_k) \ , \tag{9m}$$

where

$$\text{sign}(x) = \begin{cases} -1 \ , & x < 0 \\ +1 \ , & x > 0 \ , \end{cases} \tag{9n}$$

and the borehole is located at $t_{M/2}$. Here **H** and **T** are used for transforming p before and after fitting and differentiation, and **S** is used for transforming $\delta^3 p'$ before fitting and differentiation.

We may now define the "secondary" matrices:

$$\mathbf{M1} \equiv \mathbf{AA'},\ \mathbf{M2} \equiv \mathbf{BDS},\ \mathbf{M3} \equiv \mathbf{TEFH},\ \mathbf{M4} \equiv \mathbf{GCDS},\ \mathbf{M5} \equiv \mathbf{C'DS}, \tag{10}$$

so that Eqs. (8a) and (8b) can be written more compactly:

$$\left\{\mathbf{M1} - \frac{\alpha\Delta t}{\tau_c}\mathbf{M2}\,\Delta\,\mathbf{M3} + \frac{\alpha\Delta t}{\tau_c}\mathbf{M4}\,\Delta\,\mathbf{M3}\right\}{}^{t+\Delta t}\mathbf{P}$$

$$= \left\{\mathbf{M1} + \frac{(1-\alpha)\Delta t}{\tau_c}\mathbf{M2}\,\Delta\,\mathbf{M3} - \frac{(1-\alpha)\Delta t}{\tau_c}\mathbf{M4}\,\Delta\,\mathbf{M3}\right\}{}^{t}\mathbf{P}\ , \tag{11a}$$

or

$$\mathbf{M}^{t+\Delta t}\mathbf{P} = \mathbf{R}\ . \tag{11b}$$

As mentioned before, we need to impose two constraints on the solution ${}^{t+\Delta t}p$. The first of these is the requirement that ${}^{t+\Delta t}\delta|_{-1}^{+1} = 0$ (by analogy with closure in our dislocation density schemes), which can be realized by adding a row to **B** and **R**:

$$B_{(N+1)j} = T_j'(+1) - T_j'(-1)\,,\quad R_{N+1} = 0\ . \tag{12}$$

The second constraint is on the borehole pressure, the value of which we wish to specify. We impose this constraint by adding rows to **M** and **R**:

$$M_{(N+2)j} = \delta_{(M/2)j}\ ,\quad R_{N+2} = p_0\ . \tag{13}$$

Our procedure for computing fluid pressure and crack opening starts by evaluating the matrices in Eq. (11a); this evaluation is required only once. Then, starting with an initial pressure distribution and crack geometry, we can compute the new pressure (viz., ${}^{t+\Delta t}p$). The new crack opening is obtained from the relation:

$${}^{t+\Delta t}\delta = [(1-\alpha)\,{}^{t}\dot{\delta} + \alpha\,{}^{t+\Delta t}\dot{\delta}]\frac{\Delta t}{\tau_c} + {}^{t}\delta\ , \tag{14a}$$

where

$$\dot{\delta} = \mathbf{M5}\,\Delta\,\mathbf{M3}\,\mathbf{P}\ . \tag{14b}$$

We may then continue to compute the next pressure, and so on. Note that ${}^{t+\Delta t}\delta$ is necessarily consistent with ${}^{t+\Delta t}p$; iteration on δ^3 in $\delta^3 p'$, although rigorously needed, produces only small effects for reasonable time steps. The implicit scheme may also be formulated on the basis of local interpolation methods.[5] Although the local matrices would be simpler to generate, global interpolation offers the advantage of greater accuracy for the same number of nodal points, and it may provide more stability.

Typical results from the global formulation of our implicit integration scheme are presented in Figs. 5 through 11. These results yield great insight on the effects of the value of α, initial pressure distribution, and time-step size.

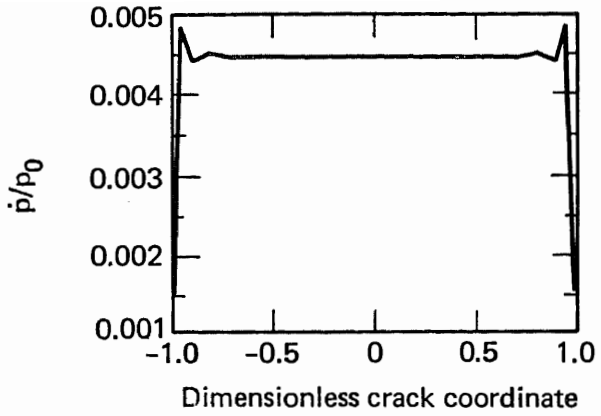

FIG. 5. Result of test of our program in which $\dot{\delta} = \sqrt{1 - x^2}$ was simulated and then integrated with γ_D via matrix operations described in the text. Result is expected constant (p/p_0) which deviates from uniformity at the tips because of errors in explicit differentiation.

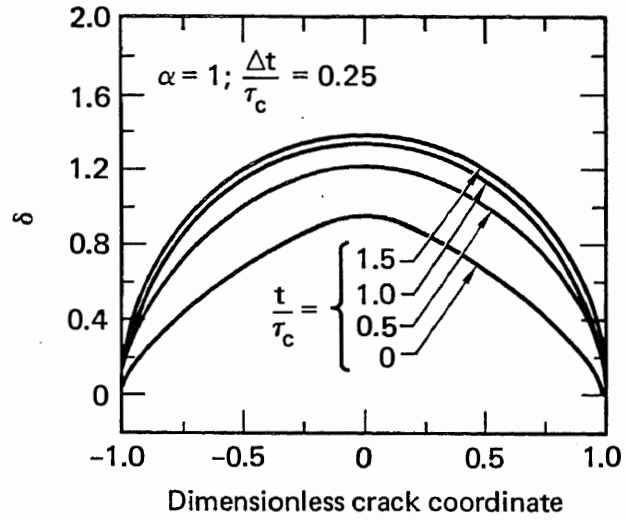

FIG. 6b. Pressure evolution curves obtained using $\alpha = 1$, $\Delta t = 0.25\,\tau_c$, $p_0/G = 1$, $\nu = 0.3$ for crack opening δ.

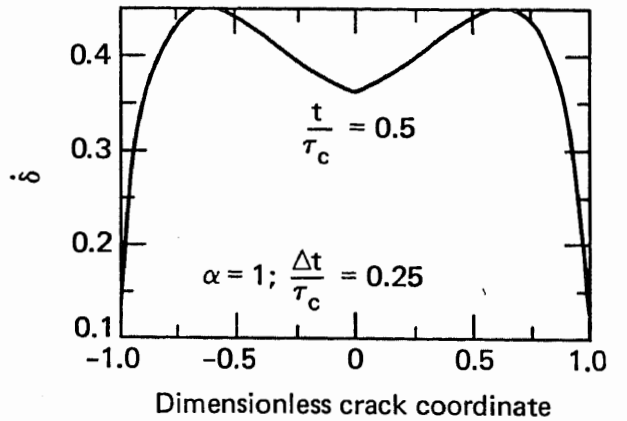

FIG. 6d. Pressure evolution curves obtained using $\alpha = 1$, $\Delta t = 0.25\,\tau_c$, $p_0/G = 1$, $\nu = 0.3$ for rate of crack opening $\dot{\delta}$.

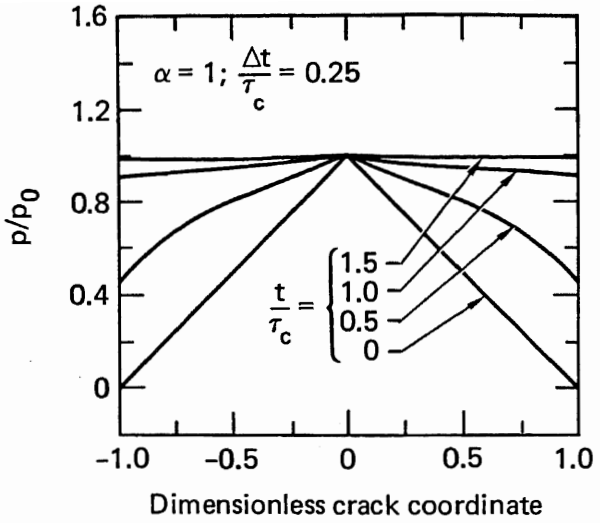

FIG. 6a. Pressure evolution curves obtained using $\alpha = 1$, $\Delta t = 0.25\,\tau_c$, $p_0/G = 1$, $\nu = 0.3$ for p/p_0.

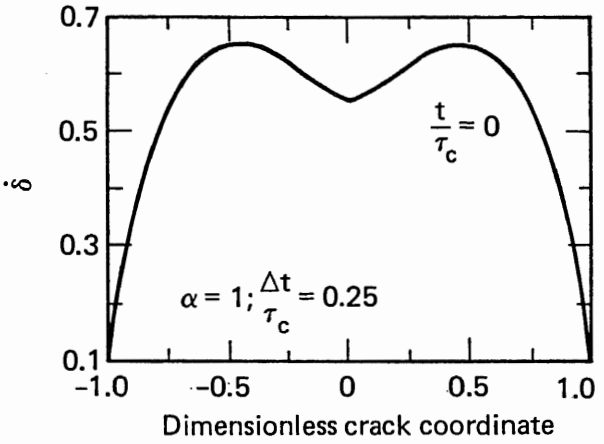

FIG. 6c. Pressure evolution curves obtained using $\alpha = 1$, $\Delta t = 0.25\,\tau_c$, $p_0/G = 1$, $\nu = 0.3$ for rate of crack opening $\dot{\delta}$.

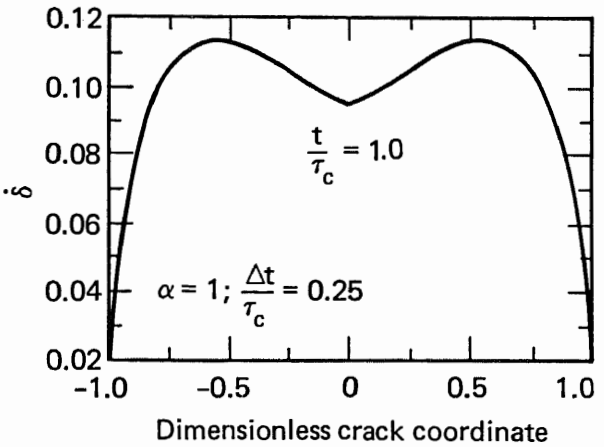

FIG. 6e. Pressure evolution curves obtained using $\alpha = 1$, $\Delta t = 0.25\,\tau_c$, $p_0/G = 1$, $\nu = 0.3$ for rate of crack opening $\dot{\delta}$.

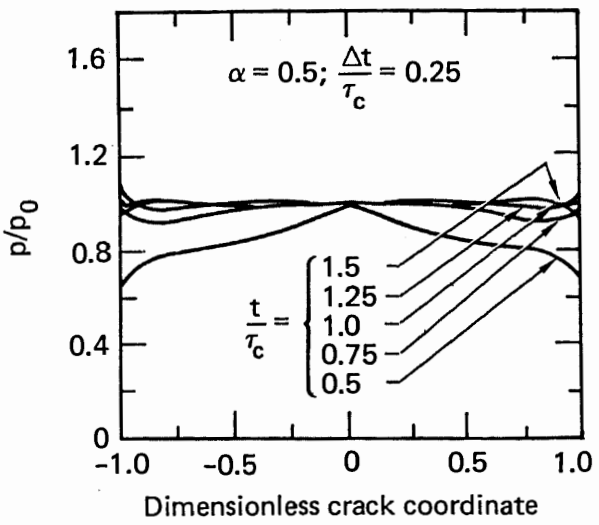

FIG. 7. Curves obtained under same conditions as those in Fig. 6 (i.e., $\Delta t = 0.25\ \tau_c$, same elastic constants, and initial pressure distribution), but with $\alpha = 0.5$. Note instability in p/p_0.

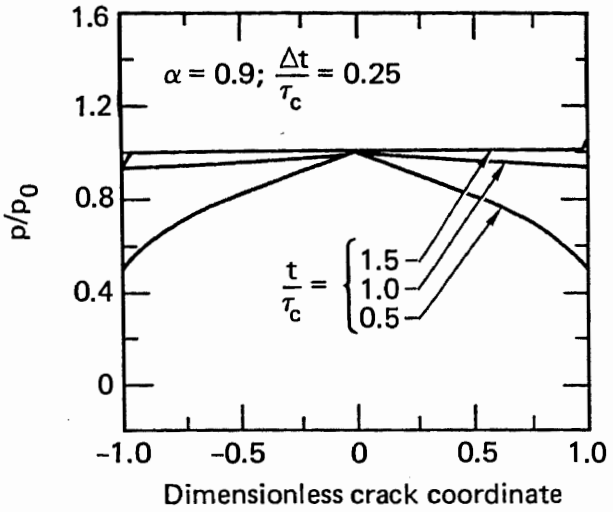

FIG. 8. Again, p/p_0 is shown with only α changed to $\alpha = 0.9$ from Fig. 6; only slight instability at $t = 1.5\ \tau_c$ occurs, but it is apparent that the best results are obtained with $\alpha = 1$ (e.g., in Fig. 6).

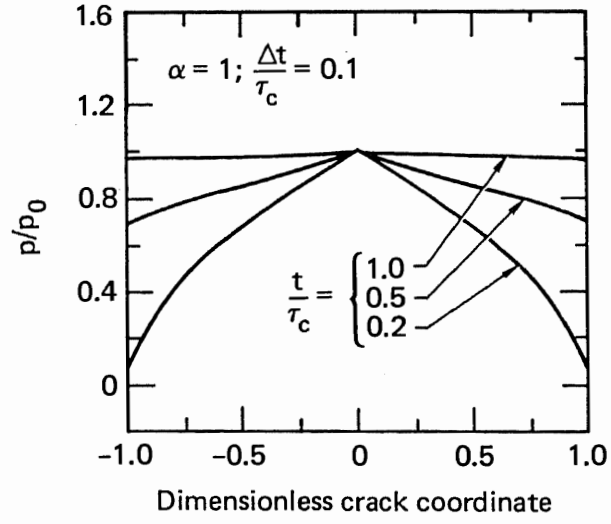

FIG. 9. These p/p_0 curves obtained with $\Delta t = 0.1\ \tau_c$, but otherwise under same conditions as for Fig. 6; e.g., $p_0/G = 1$, $\nu = 0.3$, $\alpha = 1$. Time steps of $\Delta t = 0.1\ \tau_c$ or less are necessary for all but rough calculations.

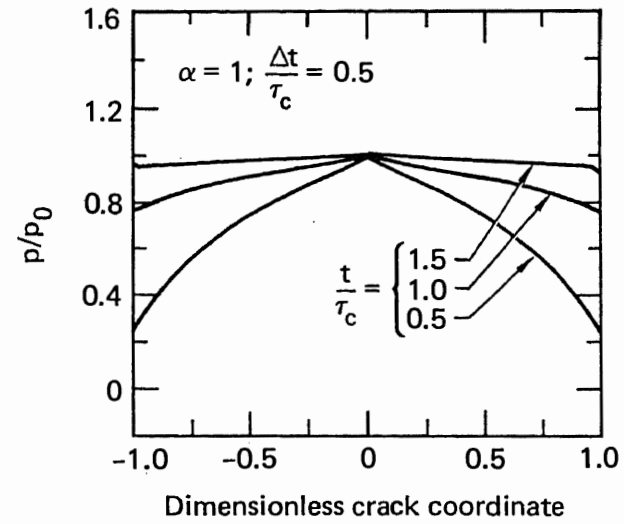

FIG. 10. Plots showing p/p_0 obtained with large time step-size ($\Delta t = 0.5\ \tau_c$), but otherwise under the same conditions as for Fig. 6. (Plots demonstrate stability of implicit scheme.)

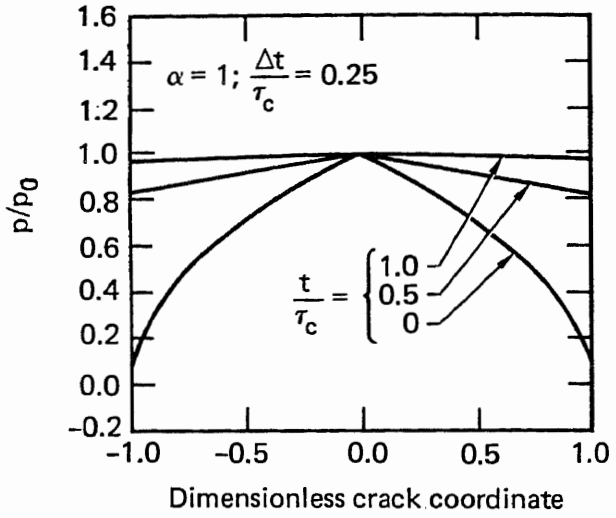

FIG. 11a. Plots showing p/p_0 for a different initial pressure distribution [$p(x,t=0) = \sqrt{1+|x|}$]. Note the reversal in curvature of p/p_0 near the borehole after $t = 0$ and the more rapid approach to uniform pressure than is obtained with a triangular initial pressure distribution. Again, $\Delta t = 0.25\ \tau_c$.

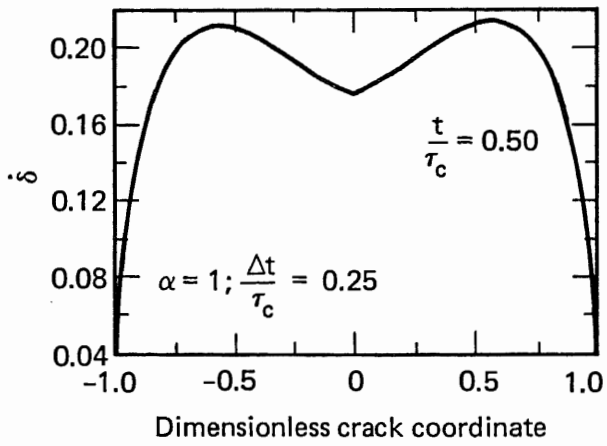

FIG. 11b. Plots showing $\dot{\delta}$ for a different initial pressure distribution [$p(x,t=0) = \sqrt{1+|x|}$]. Note the reversal in curvature of p/p_0 near the borehole after $t = 0$ and the more rapid approach to uniform pressure than is obtained with triangular initial pressure distribution. Again, $\Delta t = 0.25\ \tau_c$.

Figure 5 shows the result of a preliminary validation of the FORTRAN coding of our algorithm, especially the formulation and computation of the matrices in Eq. (9). By using $p(t_s) = t_s$, $\delta^3(t_s) = 1/2 \sin^{-1}(t_s) + 1/2\, t_s \sqrt{1 - t_s^2}$ and replacing **H**, **S**, and **T** with identity matrices, we have $[\delta^3 p']' = \sqrt{1 - t_s^2}$, which, when integrated with γ_D, should produce a constant p. This curve, while constant over most of the interval (−1,1), has "spikes" at both ends that are apparently the result of slight inaccuracies in the explicit computation of the various derivatives. We plan to remedy this, but it has not caused any serious perturbations in our remaining computations.

Figure 6 shows a set of pressure evolution curves, obtained with $\alpha = 1$ and $\Delta t = 0.25\ \tau_c$, in which the borehole pressure is maintained at a constant level at each time step. As is the case for all other figures except Fig. 11, it starts from the triangular pressure distribution shown in Fig. 5. We note that, near the borehole, p has the positive curvature necessary to produce an ever increasing crack opening at the borehole (since $\delta = (\delta^3)' p' + \delta^3 p'$), which is consistent with the continuous addition of fracture-fluid. At $t = 1.5\ \tau_c$ the fluid pressure becomes essentially constant over the crack length, verifying that τ_c is an excellent estimate of the time required for pressure penetration to the crack tips. Also, at $t = 1.5\ \tau_c$ we note that the crack opening is very close to the analytical result $\delta = \sqrt{1 - x^2}$ that we would expect from a uniform pressure.

Figure 7 shows results of computations similar to those in Fig. 6 except that we have chosen $\alpha = 0.5$, bringing ${}^{t+\Delta t}p$ under the influence of the requirement of mass conservation at time t. The effect is that the algorithm tends to become unstable for t near τ_c. Similar calculations with $\alpha = 0.9$ produced the results shown in Fig. 8. The solutions exhibit nearly as much stability as for $\alpha = 1$. We thus conclude that, in general, the best results are to be obtained when $\alpha = 1$ and that there is little computational advantage to using $\alpha < 1$.

The effect of changing the time-step size is shown in Figs. 9 and 10 along with the previous results (Fig. 6). Comparison reveals that there is enough difference between the curves obtained by various step sizes to warrant the use of $\Delta t \simeq 0.10\ \tau_c$, or smaller.

Figure 11 shows the effect of using a different initial pressure distribution, in this case $p(x,t=0) = \sqrt{1 + |x|}$ rather than the triangular distribution used in the other cases. Two phenomena are noteworthy: first, the pressure reaches an essentially uniform value more rapidly ($1.25\ \tau_c$ vs $1.5\ \tau_c$), and as

well, the negative (adverse) curvature of the initial pressure curve has reversed by time 0.25 τ_c. The latter observation provides evidence that we can start with a variety of initial distributions and be assured of stability of the solution, and that the various pressure distributions will quickly tend towards the same shape with ongoing time.

Our next task will be to develop the capability of simulating a fracture-fluid front moving toward the crack tip (allowing a study of the associated pressure evolution). Then we will proceed to model the actual crack propagation, as necessitated by a finite allowable stess-intensity factor at the tip. The equations we have formulated for these analyses do not contain appreciable increases of complexity over the equations and solutions just presented; indeed, only small modifications are needed.

NUMERICAL SOLUTION OF THREE-DIMENSIONAL CRACK PROBLEMS BY LOCAL INTERPOLATION PROCEDURES

Consider a three-dimensional plane crack with arbitrary shape, as shown in Fig. 12. We have established that such a fracture geometry can be represented by a continuous distribution of three pairs of mutually orthogonal force dipoles as shown inset in Fig. 12.[9] Such a combination of dipoles arises from the recognition of the tensile crack as a distribution of nuclei of effectively infinite one-dimensional strain, such that integration through the vanishing crack thickness gives the actual opening displacement $\delta(x_1, x_2)$. This basic unit of the model for the fracture event will be referred to as the "tensile dipole" hereafter. The appropriate influence function for such a tensile dipole can be obtained readily from Kelvin's solution for a point force in an infinite elastic medium. Taking the x_3-axis to be parallel to the force dipole with strength T, the stresses σ_{ij} at a point (x_1, x_2, x_3) due to a tensile dipole at (ξ_1, ξ_2, ξ_3) are:

$$
\begin{aligned}
\sigma_{ij} = -\frac{T}{8\pi(1-\nu)r^3}\Bigg(&\frac{3(x_i-\xi_i)(x_j-\xi_j)}{r^2}\Bigg\{5\left[\frac{(x_3-\xi_3)^2}{r^2}+\frac{\nu}{1-\nu}\frac{(x_1-\xi_1)^2}{r^2}\right.\\
&\left.+\frac{\nu}{1-\nu}\frac{(x_2-\xi_2)^2}{r^2}\right]-\left(1+\frac{2\nu}{1-\nu}\right)\Bigg\}\\
&-\frac{6\nu(x_3-\xi_3)}{r^2}[(x_i-\xi_i)\delta_{j3}+(x_j-\xi_j)\delta_{i3}]\\
&-\frac{6\nu^2(x_1-\xi_1)}{(1-\nu)r^2}[(x_i-\xi_i)\delta_{ji}+(x_j-\xi_j)\delta_{i1}]\\
&-\frac{6\nu^2(x_2-\xi_2)}{(1-\nu)r^2}[(x_i-\xi_i)\delta_{j2}+(x_j-\xi_j)\delta_{i2}]\\
&-(1-2\nu)\Bigg\{\frac{3\delta_{ij}}{r^2}\left[(x_3-\xi_3)^2+\frac{\nu}{1-\nu}(x_1-\xi_1)^2+\frac{\nu}{1-\nu}(x_2-\xi_2)^2\right]\\
&-\delta_{ij}\left(1+\frac{2\nu}{1-\nu}\right)+2\left(\delta_{i3}\delta_{j3}+\frac{\nu}{1-\nu}\delta_{i1}\delta_{j1}+\frac{\nu}{1-\nu}\delta_{i2}\delta_{j2}\right)\Bigg\}\Bigg)\quad,
\end{aligned}
\tag{15}
$$

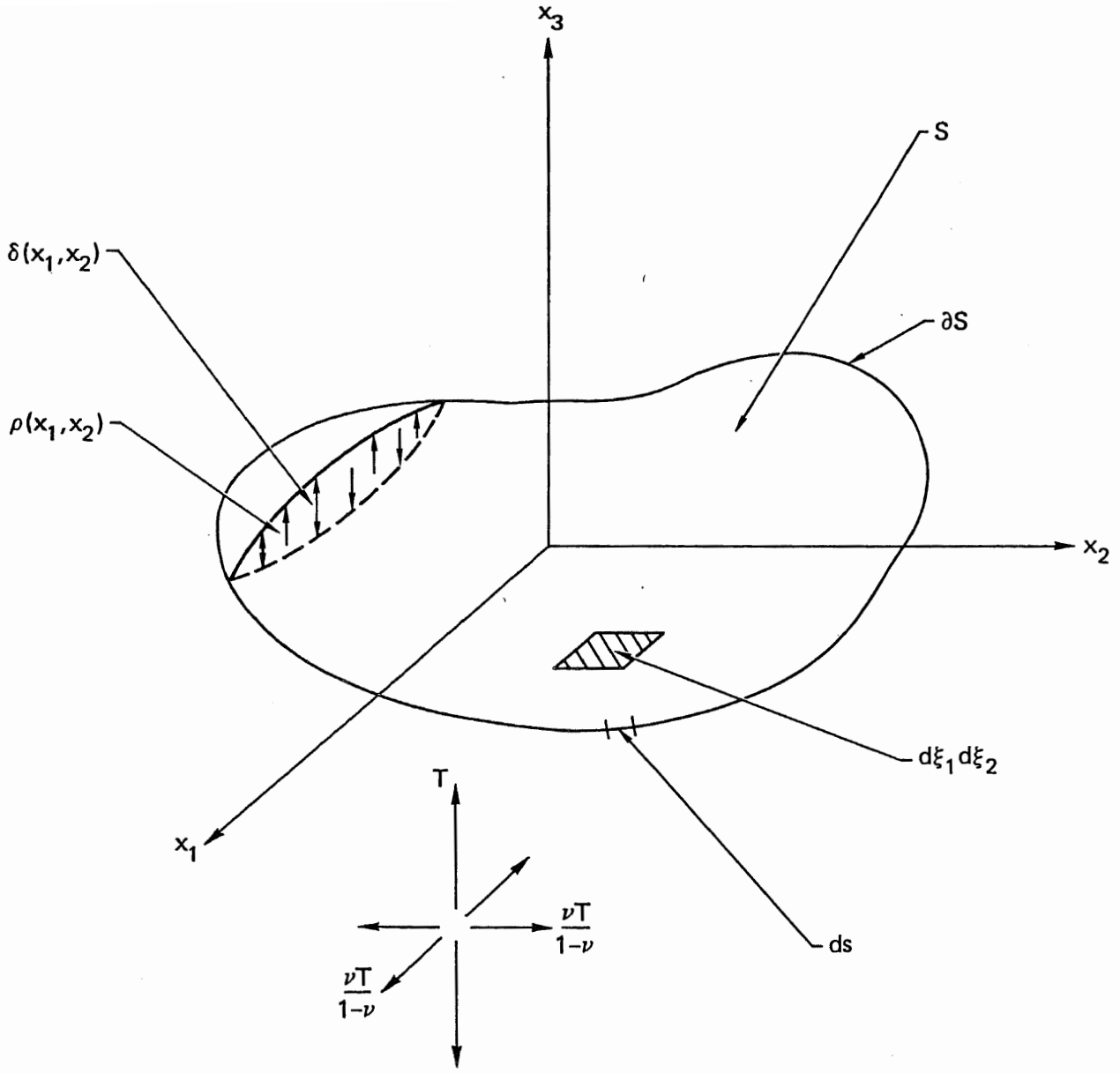

FIG. 12. Crack geometry and loading. Shown inset is the tensile dipole used as a basic influence function for three-dimensional cracks in isotropic medium; completely analogous representation for anisotropic medium.

where $r^2 = (x_i - \xi_i)(x_i - \xi_i)$ and T is the strength of the tensile dipole.

When we take the plane of the crack to be normal to the x_3-axis, the stress component of interest is σ_{33}. Also, we will be evaluating σ_{33} on the crack surface from tensile dipoles on the same surface, so that $x_3 = \xi_3 = 0$. Thus Eq. (15) reduces to:

$$\sigma_{33} = C_1 T/r^3 , \quad C_1 \equiv (1 - 2\nu)/8\pi (1 - \nu)^2 , \tag{16}$$

where $r^2 = (x_1 - \xi_1)^2 + (x_2 - \xi_2)^2$ expresses the planar radial position from the dipole.

By distributing an unknown density, $\mu(x_1, x_2)$, of these tensile dipoles over the whole plane S_T, containing the crack surface, and equating the known pressure distribution acting on the crack surface to that produced by the distribution of tensile dipoles, we obtain:

$$p(x_1, x_2) = - \iint_{S_T} \frac{C_1}{r^3} \mu(\xi_1, \xi_2) d\xi_1 d\xi_2 , \tag{17}$$

where $p(x_1, x_2)$ is the pressure acting on the crack surface and the signs for $p(x_1, x_2)$ are taken to be positive in the sense shown in Fig. 12.

The relevant tensile dipole density, $\mu(\xi_1, \xi_2)$, can be expressed in terms of the crack opening $\delta(x_1, x_2)$ as:

$$\mu(\xi_1, \xi_2) = \frac{2G(1 - \nu)}{1 - 2\nu} [\delta(\xi_1, \xi_2) - \delta(x_1, x_2)] . \tag{18}$$

The reason for introducing (x_1, x_2) as reference is that the influence at a point (x_1, x_2) from another point (ξ_1, ξ_2) is due to the *difference* of the openings at the two points. This is appreciated by recognizing that a uniform misfit strain [with associated opening $\delta(x_1, x_2)$] over the whole plane S_T would produce zero stress at all points, and at (x_1, x_2) in particular. The constant of proportionality in Eq. (18) can be obtained by considering the stress required to produce a uniaxial misfit strain, corresponding to the crack opening. Effectively, $\mu/\Delta x_3$ is equated to the uniaxial straining modulus times the effective misfit strain $[\delta(\xi_1, \xi_2) - \delta(x_1, x_2)]/\Delta x_3$. Equations (17) and (18) together give:

$$p(x_1, x_2) = - \iint_{S_T} \frac{C_2}{r^3} [\delta(\xi_1, \xi_2) - \delta(x_1, x_2)] d\xi_1 d\xi_2, \quad C_2 \equiv \frac{G}{4\pi(1 - \nu)} . \tag{19}$$

Alternatively, Eq. (19) can be written as:

$$\frac{P}{C_2} = - \iint_{S} \frac{1}{r^3} [\delta(\xi_1, \xi_2) - \delta(x_1, x_2)] d\xi_1 d\xi_2 - \delta(x_1, x_2) \oint_{\partial S} \mathbf{n} \cdot \nabla_\xi \left(\frac{1}{r}\right) ds , \tag{20}$$

where ∇_ξ is the two-dimensional gradient operator with respect to ξ_1, ξ_2; $\mathbf{n}$ is the unit vector normal to the boundary of the crack ∂S. The Green's theorem has been employed to rewrite the surface integral of $[\delta(\xi_1, \xi_2) - \delta(x_1, x_2)]/r^3$ over $S_T - S$ as a line integral along ∂S, and the vanishing of $\delta(\xi_1, \xi_2)$ outside the crack surface S has been used.

This particular result gives that equation obtained by Clifton *et al.*[10] but the method has far more general applications to inhomogeneous and anisotropic media. Also, Eq. (20) obviously reduces to Eq. (1) for two-dimensional tensile crack problems. Equation (1) was derived from a dislocation density formulation.[5]

Prompted by the success of the local interpolation scheme in two-dimensional problems[5] and also by its simplicity, we apply the scheme to Eq. (20). First, we discretize the crack into N elements (Fig. 13). In the simplest formulation, we assume a constant value for the crack opening over each element, and we collocate at N points. Thus, we obtain a system of N equations in N unknowns; namely:

$$\frac{P_i}{C_2} = - \sum_{j \neq i}^{N} \left[\iint_{S_j} \frac{d\xi_1 d\xi_2}{R_i^3} \right] \delta_j - \left[\oint_{\partial S_i} \mathbf{n} \cdot \nabla_\xi \left(\frac{1}{R_i}\right) ds \right] \delta_i , \qquad i = 1, \cdots, N,$$

$$R_i^2 = (x_1^i - \xi_1)^2 + (x_2^i - \xi_2)^2 , \tag{21}$$

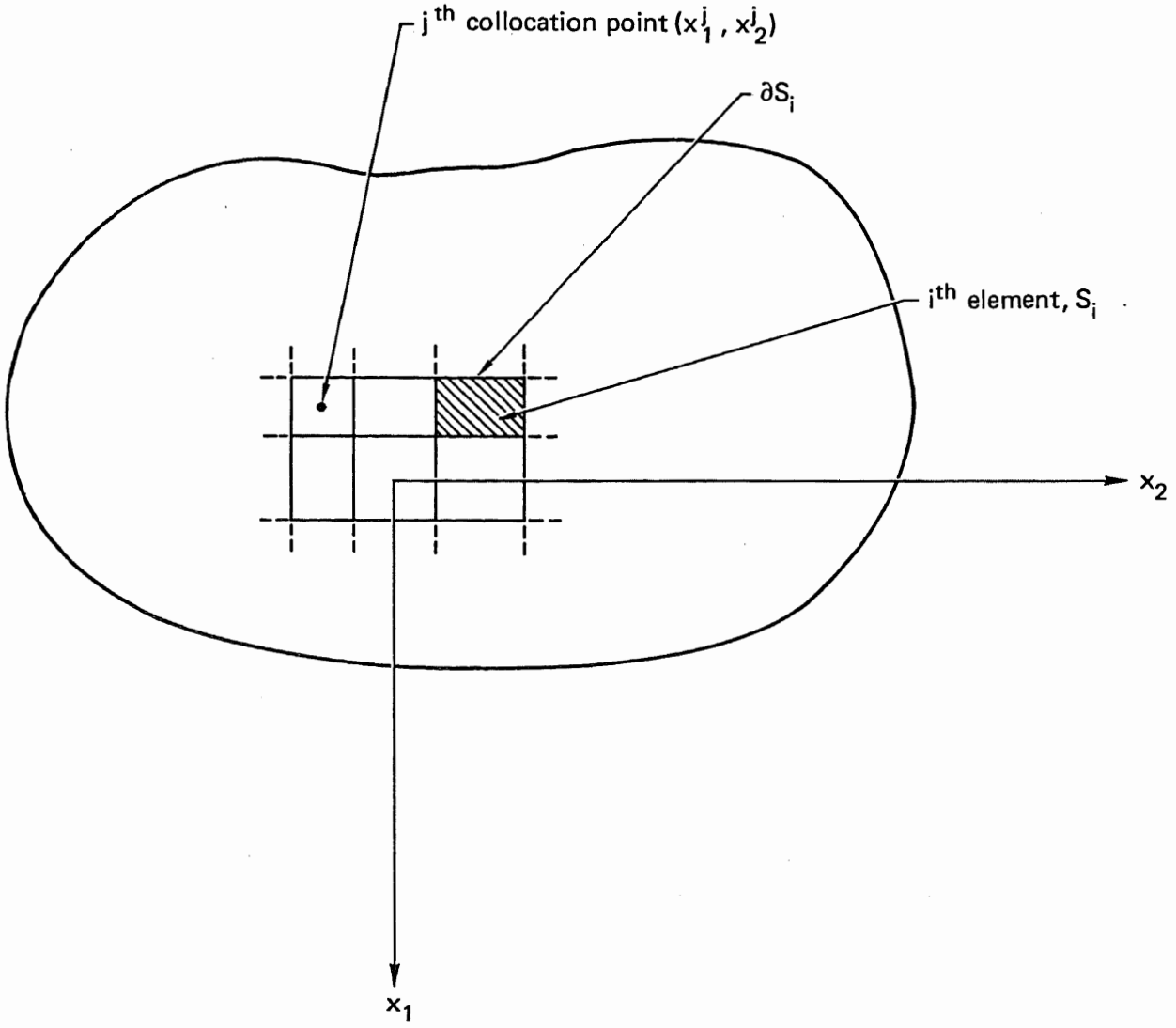

FIG. 13. Discretization of crack surface.

where (x_1^j, x_2^j) is the ith collocation point and p_i is the pressure at the same point. Notice that the surface integral in Eq. (20) vanishes for $i = j$ because of our constant interpolation function. For $i \neq j$, the $\delta(\xi_1, \xi_2)/r^3$ part of the surface integral gives us the first sum in Eq. (21). If we apply the Green's theorem to the remaining part of the surface integral in Eq. (20)—namely, $\delta(x_1, x_2)/r^3$—we obtain:

$$\iint_{S-S_i} \frac{\delta(x_1, x_2)}{r^3}\, d\xi_1\, d\xi_2 = \delta(x_1, x_2)\left[\oint_{\partial S} - \oint_{\partial S_i} n \cdot \nabla_\xi \left(\frac{1}{r}\right) ds\right]. \tag{22}$$

Thus, we see that the line integrals along ∂S cancel each other, and we are left with only an integral along ∂S_i, which is the second term in Eq. (21). This is extremely convenient because it avoids the cumbersome integration over the whole crack boundary, for each collocation point. Once the crack opening is obtained, the stress-intensity factor can be found (e.g., from Ref. 10), namely:

$$K_I(y_1, y_2) = \frac{G\delta(x_1, x_2)}{4(1-\nu)} \sqrt{\frac{2\pi}{d}}, \quad d \equiv \sqrt{(x_1 - y_1)^2 + (x_2 - y_2)^2}, \tag{23}$$

where d is the distance from (y_1, y_2) to (x_1, x_2) along the normal to the crack edge at (y_1, y_2).

The numerical procedure was tested first for a square crack (side length 2a) under uniform pressure p_0. Although no analytical solution with which to compare the results is available for such a geometry, numerical data on the stress-intensity factor K_I have been produced.[11] This and the crack opening δ is expected to be slightly higher than that of a penny-shaped crack with the radius a and quite a bit lower than that of a penny-shaped crack with radius $\sqrt{2a}$. Different numbers of elements were used. A typical mesh used is shown in Fig. 14. The collocation points were imposed at the centers of the elements. The integrations in Eq. (21) were of the Gaussian type, and the openings δ_i were solved for by using a standard elimination routine. The stress-intensity factor K_I along the side of the square was then obtained by using Eq. (23). Results are summarized in Table 1 and Fig. 15.

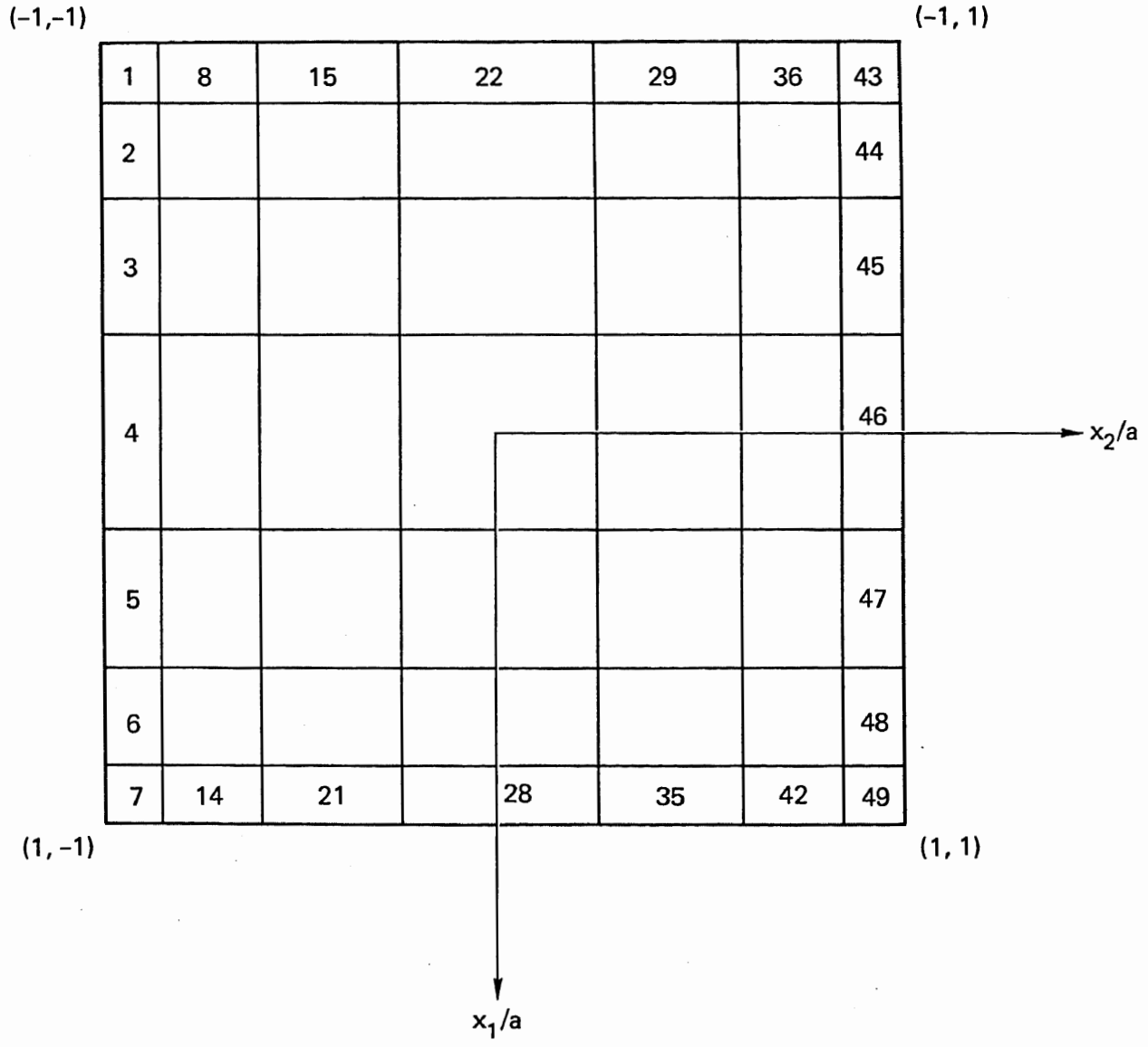

FIG. 14. Typical mesh used in square-shaped crack.

Table 1. Crack opening displacement at center of square-shaped crack and upper bound on its percent error tabulated against number of elements.

Number of elements	Opening displacement at center $\frac{G\delta_c}{4\pi(1-\nu)ap_0}$	Upper bound on percent error in δ_c (%)
1	0.17678	74.5
9	0.13433	32.6
25	0.12659	24.9
49	0.12261	21.0
81	0.11954	18.0
∞	0.10132-0.14329	0

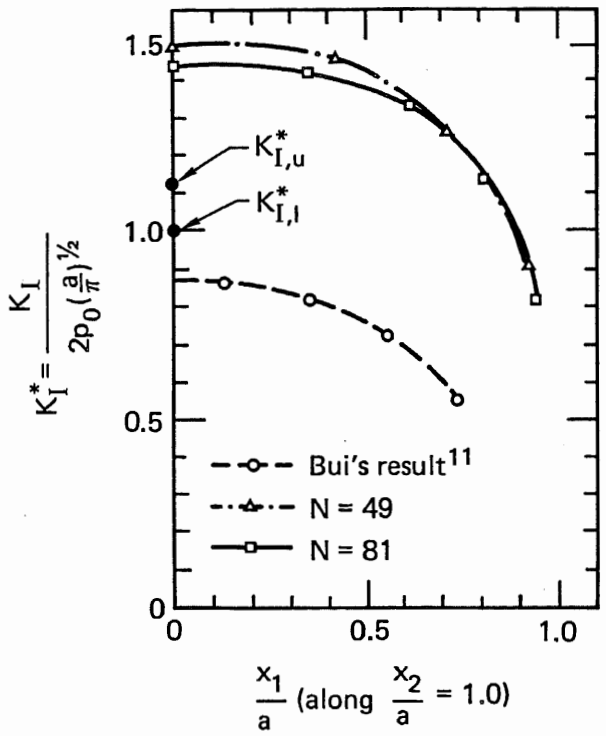

FIG. 15. Stress-intensity factor K_I^* for square-shaped crack plotted against position along one of its sides.

In Table 1 we examine the crack opening δ_c at the center. The lower and upper bounds on δ_c, provided by penny-shaped cracks of radii a and $\sqrt{2}$a, are $\delta_{c,l} \equiv 4(1-\nu)ap_0/\pi G$ and $\delta_{c,u} \equiv 4\sqrt{2}\,(1-\nu)ap_0/\pi G$, respectively. For all except a very small number of elements N, δ_c does fall within the two limits, and it tends toward $\delta_{c,l}$ as N increases. Using the lower bound on δ_c as a reference, we obtained an upper bound on the percent error in δ_c; namely:

$$\text{Percent Error} = \frac{\delta_{c,\ell} - \delta_c}{\delta_{c,\ell}} \times 100\% \ . \tag{24}$$

This quantity decreases monotonically as N increases but convergence is slow. An explanation for such a slow rate of convergence is the low order of interpolation used in approximating the crack opening δ in Eq. (20); this low order of interpolation can readily be remedied.

In Fig. 15 the stress-intensity factor K_I^*, normalized to the stress-intensity factor $K_I = 2p_0\,(a/\pi)^{1/2}$ for a penny-shaped crack of radius a, is plotted along a side of the square. As in the case of δ_c, we may also obtain lower and upper bounds for K_I^*, from inside and outside circular cracks; namely, $K_I^*{}_{,l} = 1.0$ and $K_I^*{}_{,u} = 1.1892$. These values are indicated in Fig. 15, and we observe that the calculated K_I^* has an error of approximately 40% for N = 81. Again, the fault lies with the crude interpolation used for δ. In addition, Eq. (23) is true only when d is small. Since the collocation points are at the center of each element, it is natural to take the crack openings obtained to be a representative value at the center as well. Therefore, the distance d is determined by the mesh size. This means that a finer mesh near the edge of the crack will help to improve the accuracy of the stress-intensity factor K_I^* calculated.

From the numerical results obtained we conclude that the local interpolation scheme is a satisfactory way of solving Eq. (20). A global interpolation scheme has also been suggested.[12] The latter involves a mapping of the arbitrary crack geometry onto a square. This mapping poses a problem when the crack geometry is

irregular, because irregularity introduces singularities in the mapping. On the other hand, in the local interpolation, we need only refine the mesh around the irregular part of the geometry. Also, we see an advantage of local interpolation over global interpolation for problems that involve moving boundaries, such as crack propagation problems, especially with fracture-fluid evolution. For local interpolation, we have only to add more elements to the existing mesh to account for the new boundary at each step. To update the coefficient matrix, we simply supplement the previous one with a row and a column. In global interpolation, a different mapping of the crack geometry is required at each step; moreover, the coefficient matrix must be constructed at each step as well. Since the latter requires a large amount of computation, especially by comparison with the local scheme, the balance would appear to tip in favor of the latter. However, the global interpolation scheme does give much greater accuracies than does the local interpolation scheme for a corresponding size of matrix. At this point, no firm preference can be established between the two schemes because, for the hydrofracture problem, we have not performed sufficient evaluation of relative costs and effectiveness in solution.

LABORATORY EXPERIMENTS

Experiments have been started to study hydraulic crack growth in limestone near interfaces that are intersected by cracks. This phenomenon has been modeled theoretically, and the stress-intensity factor near the tip of the pressurized crack has been computed as the crack approaches an interface that is intersected by 0, one, and two preexisting cracks.[5] To model experimentally this geometry our standard setup for the study of crack growth was modified as shown in Fig. 16. The setup consists of a sandwich of three limestone blocks, 4-in. by 4-in. by 2-in. (100-mm by 100-mm by 50-mm), with the fluid-pressurized crack initiated and driven in the center block. A load is applied so that a normal stress is set up across interfaces I_1 and I_2. In these experiments, however, the upper block consists of three blocks that are precisely machined and aligned adjacent to one another to give the effect of preexisting cracks C_1 and C_2 that intersect the interface I_1 at right angles. In an initial experiment in which the applied load, W, exceeded the threshold stress for crack growth across unbonded interfaces in limestone, ~45 MPa (~650 psi), the pressurized crack crossed the interface I_2 from the central block in which it was initiated into the lower single block but failed to cross the interface I_1, which was intersected by the two cracks C_1 and C_2. This result is consistent with the predictions of the mathematical model when the Mode 1 stress-intensity factor is used as a criterion for predicting crack growth. However, because this result is based on only one observation, it must now be considered preliminary and subject to further modification. Further experiments are planned to establish a definite trend.

REVIEW OF DATA ON EVOLUTION AND STRESS HISTORY OF SOME WESTERN GAS SANDS

The physical properties that control many of the productive characteristics of gas reservoirs are a result of original sedimentary character and the changes since deposition. These physical and chemical changes are due to burial, heat, and the effect of applied stress over time. The stress history includes compression and shear due to burial and compaction, unloading due to erosion, predominantly effective tensile stresses during uplift, and a wide range of compressive and shear effects—all caused by tectonic processes.

Stratigraphy and stress history are important for several reasons. Reservoir behavior is in part a function of original permeability as modified by natural and artificially induced fracturing. Original permeability is a function of the stratigraphic-tectonic environment at deposition. Natural fracturing is a result of past stress history, and artificial fracturing is in part controlled by mechanical properties including discontinuities, and by the present state of stress in the rock. Analyses of the stratigraphy and the stress history of reservoirs should assist in interpretation of well logs, geologic and geophysical data, and field production

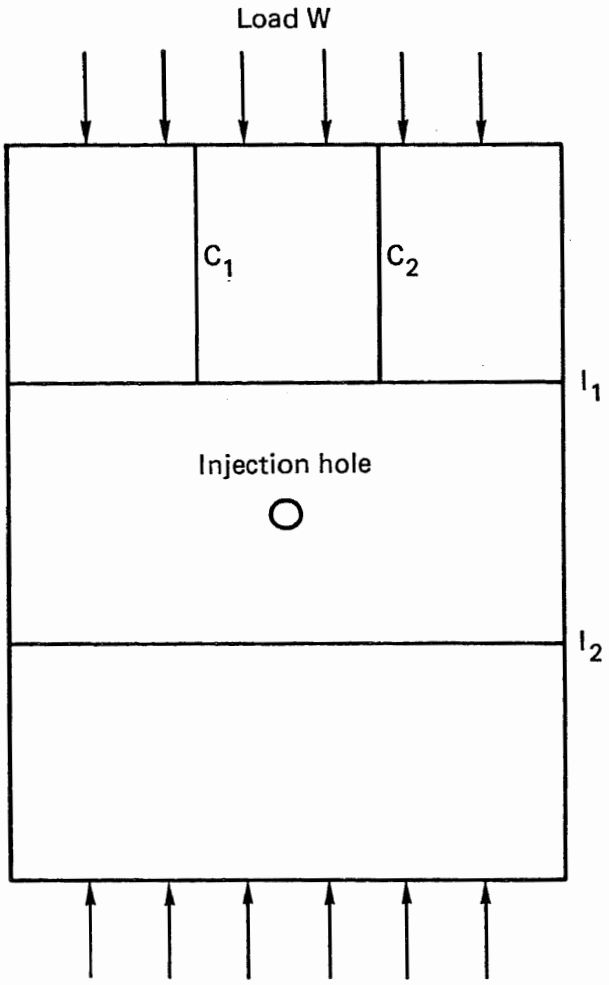

FIG. 16. Experimental setup to study crack growth near interfaces that are intersected by cracks c_1 and c_2.

data. Moreover, analyses can help us to understand reservoir behavior and to design fracture and other stimulation techniques.

The area of the Wind River, Green River, Uinta-Piceance basins of the Rocky Mountain foreland, and the San Juan basin is suited to such an analysis because of abundant surface and subsurface data and intensive fuel and mineral development that has produced a very large number of structural and stratigraphic studies and analyses.[13]

PROCESSES

The processes involved can be described generally as:

- Deposition
- Burial and early diagenesis
- Tectonism
- Thermal and metamorphic processes
- Erosion and uplift.

These processes may be repeated in whole or in part, and commonly have been repeated in the older rocks. The following paragraphs present a brief discussion of the processes and possible implications as they apply to the Mesaverde and related rocks in the central Rocky Mountain area.

DEPOSITION

This discussion is limited to the Mesaverde type rocks of the Upper Cretaceous Montana Group, the regressive sandstone tongues of Weimer's regressive cycles R_2 and R_3.[14] These rocks produce gas and oil in the Wind River, Green River, Uinta-Piceance, and San Juan basins. They are often of low permeability and, for commercial production, require artificial fracturing.

The reservoir sandstones are generally poorly sorted and in discontinuous bodies deposited in a shoreline or near-shore environment.[15] The sand bodies are the result of repeated advance and retreat of the western shore of the Late Cretaceous Sea. The source of sediment was to the west; the environment changes from marine to coaly to alluvial nonmarine in a westward direction. The greatest thickness of these rocks and the most sandy sections are generally in the location of the present Green River and Piceance basins. Equivalent rocks in the San Juan basin are generally thinner. The sedimentary environment results in reservoir units of limited extent encased in less permeable sediments.

BURIAL AND EARLY DIAGENESIS

Thickness is generally a function of rate of deposition; thicker sections of rock probably underwent earlier burial, compaction, and first-stage diagenesis. Rapid burial may promote early failure along steeply dipping shear planes in the immature sediments.

TECTONISM

The region was generally subject to compression in an east-west direction before deposition of the Upper Cretaceous sediments. This compression resulted in mountains to the west that were the source of the coarse sediments, in the formation of the depositional basins, and ultimately in the overthrust belt to the west and the major folds and faults of the Rocky Mountain foreland referred to as the Laramide orogeny. The detailed mechanics were complex; the general east-west compression was modified by local and inherited structures.[16–18] Unmodified compressive stress in rocks at depth would tend to promote near vertical fracturing.

THERMAL AND METAMORPHIC PROCESSES

The depositional basins of interest have had little intrusive or extrusive igneous history since Late Cretaceous time. This is in marked contrast to adjoining regions; e.g., the Colorado mineral belt, the Absaroka-Yellowstone region, and the Snake River plain. Present heat-flow is minimal[19]—again in contrast to some neighboring areas. We can conclude that any thermal metamorphism, which is low in the particular regions of interest, will be due to deep burial rather than to igneous activity. We would expect that areas with the thickest Upper Cretaceous and younger rocks (i.e., the Green River and Piceance basins) would have more effects of deep burial.

EROSION AND UPLIFT

The post-Paleocene history of the region includes both erosion and uplift followed by downwarp and deposition. The modern state is one of uplift and erosion. This state is the final stage in a series including Eocene deposition, then erosion, followed by Late Tertiary deposition, and a final uplift cycle. Uplift and erosion may promote tensional fracturing and finally a state in which the minimum principal stress is vertical, and near-horizontal jointing develops. Because burial may change the stress state again, maximum pressure is

vertical and high-angle shears and vertical tension fractures develop. In this deposition/downwarp, uplift/erosion, deposition/downwarp cycle, several distinct sets of shear and tension fractures could develop. Figure 17 illustrates some possible relationships between fractures, simple stress regimes, and some simple stratographic units. With underlying or inherited structures and local discontinuities in rock properties, the detailed picture may become very complicated. In any event, the rock, its discontinuities including fractures, and the present state of stress are the end result of this history.

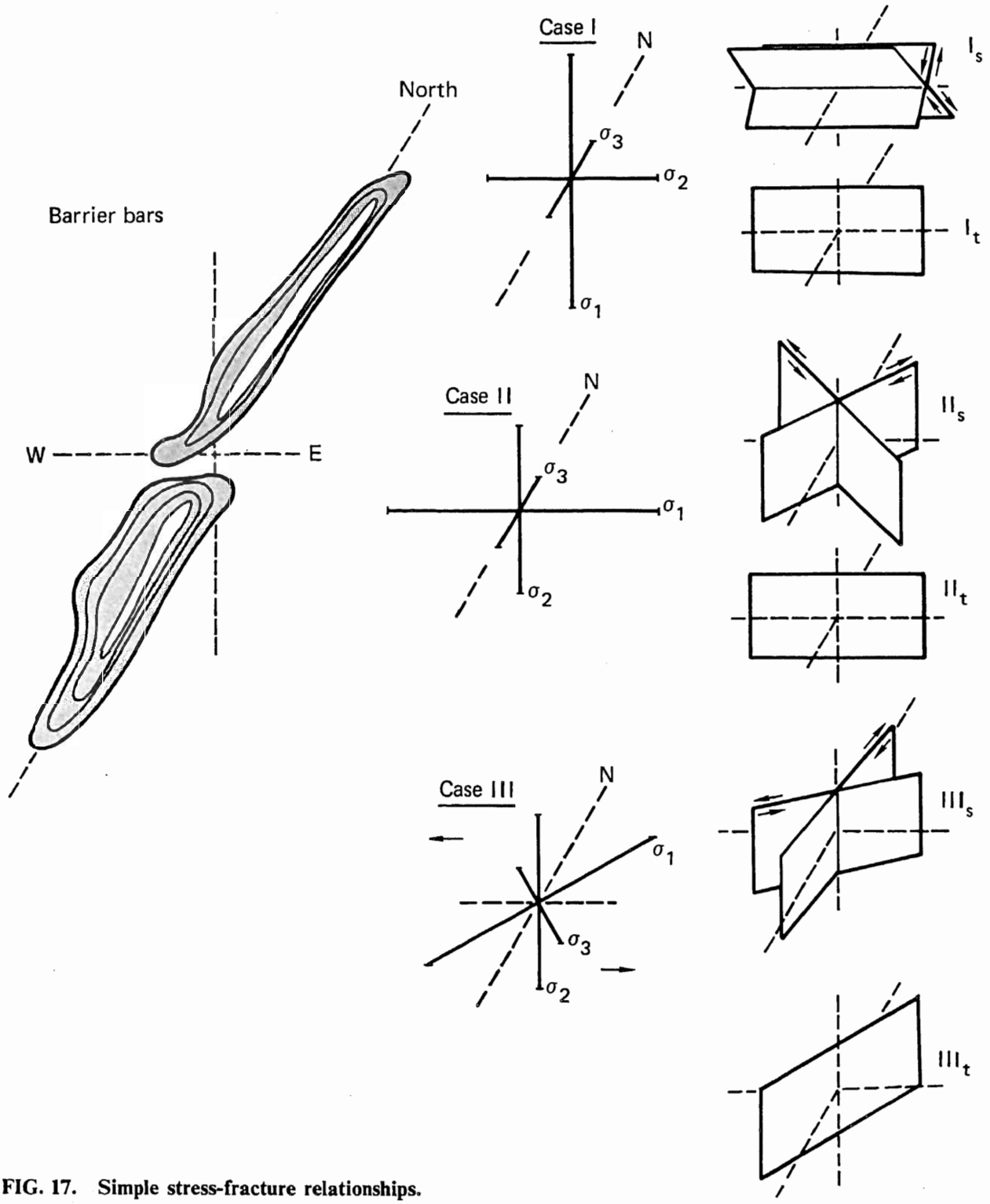

FIG. 17. Simple stress-fracture relationships.

Figure 17 illustrates the possible relationships between the fractures produced by three simple stress regimes and the orientation of typical barrier bar sand bodies, such as those in the Almond Formation on the Wamsutter Arch in the Green River basin of Wyoming. In the figure, σ_1 is the maximum principal stress direction (stress taken as compressive), σ_2 is medium principal stress, and σ_3 is the least principal stress.

- Case I is simple subsidence and compaction, where maximum stress is vertical. Steeply dipping shears (I_s) and vertical tension fractures (I_t) may develop, with an east-west strike. These shears and fractures cut across the small dimension of the sandstone barrier bar reservoir.
- Case II has maximum stress horizontal in an east-west direction. Preferred shear directions are northeast-southwest and northwest-southeast, with relative movement as shown by the arrows (II_s). These fractures cut the bars at an acute angle but might serve to connect them across the channel in the middle. Tension fractures (II_t) are again vertical and east-west.
- Case III has maximum compressive stress in a horizontal and northeast-southwest direction, which stress could be the result of an east-west left-lateral shear couple as shown. This orientation could produce one set of shears almost parallel to the long dimension of the bars (III_s). The tensional fractures (III_t) are rotated so that they cut the bars at an acute angle and could serve to connect across the middle channel.

In summary, understanding the sedimentary features and their relation to the stress-induced changes may aid in the analysis of oil and gas reservoirs and the design of stimulation treatments. For example, it may be possible from geologic data to predict where natural fractures parallel the long dimension of the reservoir unit. Or this information may be used to form new fractures that do the same thing.

Tectonic and stress-history investigation should be continued along these lines:

- Compilation of regional, basin, and field scale data on stratigraphy, structure, and tectonics
- Development of theoretical stress analyses from the above
- Checking of these against available information on mechanical properties, including fractures and *in situ* stress measurements
- Development of new information if required
- Correlation of stratigraphic and mechanical data against reservoir and well performance.

The results should be useful in predicting reservoir behavior, in designing and interpreting well logging and testing programs, and ultimately in field development and stimulation programs.

LOGGING

In a previous report[20] we discussed the digitization of the coda of a variable-intensity-recorded continuous-velocity log. We associated dips in a contour of amplitude of this coda (signifying that the signal of a given amplitude had died away at an earlier time) with gas shows. This digitization process is slow, costly, and inaccurate, and has never been repeated.

Another logging contractor ran a similar log in another hole (Columbia Gas No. 20403) at the same site. The sonic tool used in this well had a much longer source-detector spacing, 25 m instead of 1 m (8 ft instead of 3 ft), but there were four detectors and the amplitude vs time for these detectors was digitized and taped. Recently we wrote a computer program to read these tapes and to plot a color variable-intensity log. Samples of sections of this log are shown in Figs. 18 and 19. The vertical axis is depth, and the horizontal axis is time out to 5 ms, and therefore does not show the entire coda (the log discussed above had time out to 20 ms and did show all of the coda). Amplitude of the signal is represented by color. Black signifies negative amplitude, green near-zero amplitude (both positive and negative), and the other colors represent positive amplitudes as shown in the callout. The maximum possible amplitude is 2048.

In Fig. 18 we see a pair of magenta lines between 3990 and 4010 ft that seem to be caused by a water wave reflected from a feature intersecting the hole (or caused by a change in hole size—but the caliper gives no indication of such a change). These lines are visible on an ordinary black and white plot of this log. But another feature, starting at about 3940 ft at 5 ms and continuing to about 3950 ft at 3 ms, would not be visible in the ordinary log.

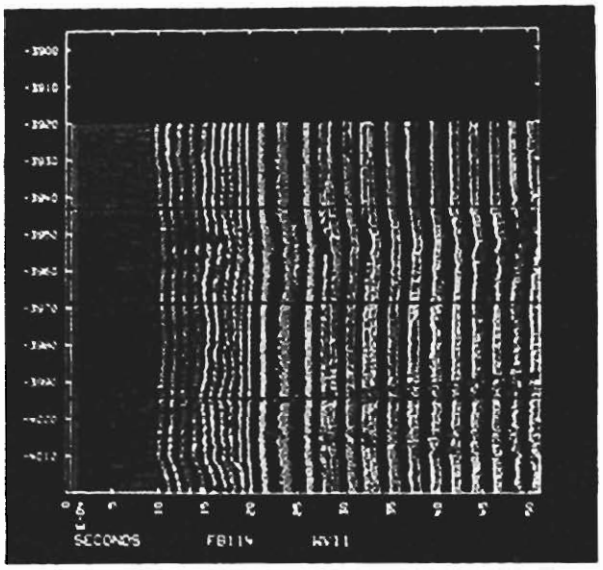

FIG. 18. Part of color-variable-intensity-recorded continuous-velocity log. Vertical axis represents depth in feet; horizontal axis, time in seconds. Amplitude of acoustic signal is represented by colors: green signifies near-zero amplitude, both positive and negative; black signifies appreciable negative amplitude; on a scale of 0 to 2048, yellow signifies positive amplitudes between 100 and 400, blue between 400 and 700, cyan between 700 and 1000, red between 1000 and 1500, and magenta greater than 1500.

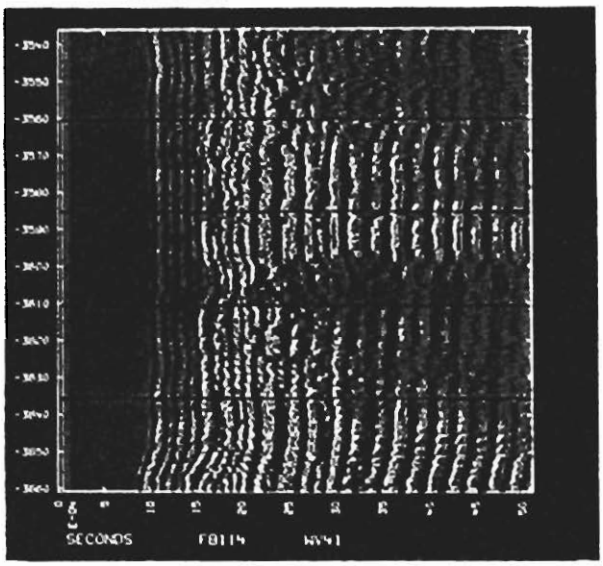

FIG. 19. Part of color-variable-intensity-recorded continuous-velocity log; significance of colors is same as in Fig. 18.

Figure 19 shows a low-amplitude region extending over much of the section, but this low amplitude does not appear until approximately 2 ms. An ordinary amplitude log of this hole shows only the changes in amplitude of the first few cycles. This low-amplitude region seems to be associated with gas shows on a sibilation log, with a dip in the sibilation signal in the region near 3590 ft where the acoustic amplitude increases. However, other gas shows in the sibilation log are not associated with low-amplitude regions in this color log. Perhaps, were the entire coda available, such regions could be found, but this is still a matter for conjecture.

We believe that a shorter transmitter-receiver distance will also be more satisfactory in locating fractures. In the near future we hope to be able to obtain logs with shorter transmitter-receiver distances and longer sweeps. We then will be able to learn whether this technique will help to locate fractures.

ROCK MECHANICS MEASUREMENTS

Our rock mechanics measurements activity during the quarter includes:

- Completion of the Brazilian Test (tensile strength) of the Mesaverde sandstone from Sublette County, Wyoming. The specimens were loaded either perpendicular or parallel to bedding.
- Completion of the specimen preparation of the Wyoming Mesaverde sandstone for the other planned equation of state studies.
- Initiation of the pressure-volume measurements for the Mesaverde sandstone and shale from Rio Blanco County, Colorado.
- Completion of assembling the high-pressure vessel for simultaneous ultrasonic velocity measurements in multiple directions. A protective cover for the high-pressure system was fabricated.
- A visit to the drill site of Well No. Federal 22-12, Rio Blanco County, Colorado, to select the samples of Mesaverde shale and sandstone from the depth of approximately 1980 m (6500 ft). The Mesaverde samples that we have been studying were from the Twin Arrow well at a depth of approximately 365 m (1200 ft) in the same county. The samples selected during that visit had been received.

Current methods for predicting fracture intensity, geometry, and extent resulting from fracturing stimulation (using either high explosive or hydraulic means) of an initially impermeable natural-gas-bearing rock require certain equation of state measurements as input data to the calculation codes. In the previous quarter we began to generate the required equation of state data for Mesaverde sandstone (reservoir rock) and shale (source rock) core sections (10.16-cm-diam) from the Federal No. 24-19 well in Sublette County, Wyoming. The depth of sample origin ranged from 1579.9 to 1582.8 m.

The core sample contains alternating sections of sandstone, shale, and the mixture of the two. Both sandstone and shale sections are quite homogeneous. The bedding planes between sandstone and shale are horizontal (perpendicular to the axis of the core sample). However, within the sections of pure sandstone or shale, the bedding is not obvious. The colors of the sandstone and shale are light gray and dark gray, respectively. The sandstone is very fine grained.

To date we have completed the Brazilian test for the Wyoming Mesaverde sandstone. The results of the Brazilian test yield tensile strengths that are summarized in Table 2. We see that the tensile strength of the Wyoming Mesaverde sandstone is almost independent of the direction of loading with respect to bedding. The Wyoming Mesaverde sandstone has a much greater tensile strength than the tensile strengths of the Colorado Mesaverde sandstone and shale reported in the previous quarterly and reproduced in the lower part of Table 2 for comparison.

Table 2. Tensile strength of Mesaverde sandstone from Sublette County, Wyoming.

Rock	Depth (m)	Number of test	Parallel(∥) perpendicular (⊥)	Averaged tensile strength at 1 standard deviation (MPa)
Wyoming sandstone	1581.6	12	∥	14.46 ± 1.24
	1582.8	11	⊥	14.31 ± 2.07
Colorado sandstone	352.7	13	∥	3.29 ± 0.56
		20	⊥	3.19 ± 0.45
Colorado shale	349.9	12	⊥	11.51 ± 3.21
	354.2	7	∥	8.83 ± 4.53

REFERENCES

1. C. R. McKee, M. E. Hanson, and R. W. Terhune, *Permeability from Single and Multiple Detonations of Explosive Charges,* Lawrence Livermore Laboratory, Livermore, CA, UCRL-78207, Rev. 1 (1976).
2. A. G. Petschek and M. E. Hanson, "Difference Equations for Two-Dimensional Elastic Flow," *J. Comp. Phys.* **3,** 307-320 (1968).
3. M. E. Hanson, A. R. Sanford, and R. J. Shaffer, "A Source Function for a Dynamic Brittle Unilateral Shear Fracture," *Geophys. J.* **38,** 364 (1974).
4. M. E. Hanson, G. D. Anderson, R. J. Shaffer, D. O. Emerson, H. C. Heard, and B. C. Haimson, *Theoretical and Experimental Research on Hydraulic Fracturing,* Lawrence Livermore Laboratory, Livermore, CA, UCRL-80969 (1978).
5. M. E. Hanson, G. D. Anderson, R. J. Shaffer, W. Lin, D. F. Towse, M. P. Cleary, and B. C. Haimson, *LLL Gas Stimulation Program Quarterly Progress Report, April through June 1979,* Lawrence Livermore Laboratory, Livermore, CA, UCRL-50036-79-2 (1979).
6. M. E. Hanson, G. D. Anderson, R. J. Shaffer, D. F. Towse, A. G. Duba, N. R. Burkhard, W. Lin, M. P. Cleary, and B. C. Haimson, *LLL Gas Stimulation Program Quarterly Progress Report, January through March 1979,* Lawrence Livermore Laboratory, Livermore, CA, UCRL-50036-79-1 (1979).
7. M. E. Hanson, G. D. Anderson, R. J. Shaffer, D. O. Emerson, R. P. Swift, K. O'Banion, M. P. Cleary, B. C. Haimson, C. F. Knutson, and C. R. Boardman, *LLL Gas Stimulation Program Quarterly Progress Report, July through September 1978,* Lawrence Livermore Laboratory, Livermore, CA, UCRL-50036-78-3.
8. M. P. Cleary, "Primary Factors Governing Hydraulic Fractures in Heterogeneous Stratified Porous Formations," American Society of Mechanical Engineers Report No. 78-Pet-47 (1978).
9. M. P. Cleary, "Fundamental Solutions for a Fluid-Saturated Porous Solid," *Int. J. Solids Structures* **13,** 785-806 (1977).
10. R. J. Clifton and A. S. Abou-Sayed, "On the Computation of the Three Dimensional Geometry of Hydraulic Fractures," AIME Paper No. SPE 7943, presented at SPE Tight Gas Symposium, Denver, CO (1979).
11. H. D. Bui, "An Integral Equations Method for Solving the Problem of a Plane Crack of Arbitrary Shape," *J. Mech. Phys. Solids* **25,** 29-39 (1977).
12. M. E. Hanson, G. D. Anderson, R. J. Shaffer, D. N. Montan, L. D. Thorson, W. Lin, B. C. Haimson, and M. P. Cleary, *LLL Gas Stimulation Program Quarterly Progress Report, October through December 1978,* Lawrence Livermore Laboratory, Livermore, CA, UCRL-50036-78-1 (1979).
13. *Geologic Atlas of the Rocky Mountain Region* (Rocky Mountain Association of Geologists, Denver, CO, 1972).
14. R. J. Weimer, "Upper Cretaceous Stratigraphy, Rocky Mountain Area," *Am. Assoc. Pet. Geol. Bull.* **44,** 1-20 (1960).
15. R. J. Weimer, "Time-Stratigraphic Analysis on Petroleum Accumulation, Patrick Draw Field, Sweetwater County, Wyoming," *Am. Assoc. Pet. Geol. Bull.* **50,** 2150-2175 (1966).
16. J. K. Sales, "Crustal Mechanics of Cordilleran Foreland Deformation: A Regional and Scale Model Approach," *Am. Assoc. Pet. Geol. Bull.* **52,** 2016-2044 (1968).
17. D. S. Stone, "Wrench Faulting and Rocky Mountain Tectonics," The Rocky Mountain Geologist **6,** 67-79 (1969).
18. J. D. Lowell, "Plate Tectonics and Foreland Basement Deformation," *Geology* **2,** 275-278 (1974).
19. D. D. Blackwell, "Heat Flow and Energy Loss in the Western United States," in Geological Society of America *Memoir No. 152* (1978).
20. M. E. Hanson, R. J. Shaffer, J. R. Hearst, G. D. Anderson, D. N. Montan, H. C. Heard, and D. O. Emerson, *Update on the LLL Gas Stimulation Program,* Lawrence Livermore Laboratory, Livermore, CA, UCRL-79587 (1977).

WTF

U.S. Government Printing Office: 1980/3—689-159/30